

**Programmable Matter II: Optimizing Logical Topology and Automating
Manufacture of a Microscale, Self-Reconfigurable Swarm Robotic System**

Sohi Patel

Academy of Science and Technology, 3701 College Park Dr., The Woodlands, TX 77384, USA

Table of Contents

1. Introduction.....	1
1.1. Background.....	1
1.2. Engineering Concentration.....	4
2. Methodology.....	6
2.1. Materials.....	6
2.2. Elastomeric Mask Preparation.....	7
2.3. Three-Axis Gantry Assembly and Automation.....	9
2.4. Metal Shell Electrodeposition.....	10
2.5. ASIC Design and Fabrication.....	11
2.6. Application Software Expansion.....	15
2.7. Magnet-Fielded Stochastic Motion.....	16
2.8. Physical Examination.....	16
2.9. Logical Topology Optimization.....	18
3. Results.....	19
3.1. Physical Characterization.....	19
3.2. ASIC Functionality.....	22
3.3. Algorithmic Modeling.....	24
4. Discussion.....	27
4.1. Analysis of Results.....	27
4.2. Limitations.....	29
4.3. Future Work.....	29
4.4. Concluding Remarks.....	31

Abstract

Millions of application-specific materials are currently in circulation, each with unique extraction, refinement, and synthesis requirements incurring severe environmental and economic costs. Programmable matter, an intelligent material able to assume a variety of structural properties on command, allows for the immediate assembly and reconfiguration of any material or mechanical device from a fixed feedstock input. A modular swarm of microrobots, each supported by electropermanent magnet actuators, was designed and manufactured by electrodepositing layers of copper, iron, and cobalt-platinum through high-precision elastomeric masks with a stepped 3-axis gantry crane. Integrated circuits were designed, testbenched, and fabricated using photolithography, ion implantation, and reactive ion etching. Microrobots exhibited high strength and speed; each held 1,000 times its weight [$H = 23.0216$, $p < 0.0001$] and low transmission rate datapaths were allowably removed. Occupying just 1 mm² of die space and transferring power and data within milliseconds of connection, circuitry was architecturally optimal and compliant. Application software was programmed to translate 3D CAD models into configuration data and simulate large-scale swarm interactions. In forms of varying size and complexity, less than 0.5% deadlocking and 0% premature energy dissipation was identified [$F(2, 21) = 19012.016$, $p < 0.00001$]. Self-reconfiguration and route optimization techniques were informed by assembly planning algorithms, which sustained 50 physical microrobots and 100,000 in simulation. The developed programmable matter system boasts high functionality, robust, data-efficient algorithms, and a streamlined, scalable fabrication process flow; it can contribute impressively to issues in aerospace, defense, and infrastructure as an instrument of instant and autonomous conception.

1. Introduction

1.1. Background

The technology of today is tremendously limited by the meager variety of materials available for use. Present generations of materials are either natural to Earth or synthesized with natural materials [1], and as humanity's needs expand, stores of natural resources increasingly deplete and tire. Considering the countless, unique pieces of technology in production today, the stagnation of natural properties has begun to directly restrict the use case of each material [2]. Rapidly advancing issues in fields like energy, aerospace, and defense suffer from a ceiling on the ability to alter material properties [3]. The invention of an intelligent, dynamic material could infinitely expand the range of natural properties like elasticity and permittivity, actualize synthetic properties like superreflectance and supercapacitance [4], and introduce immediate physical adaptability to a number of tools, such as radio antennas and airplane wings [3].

Programmable matter is any intelligent material able to dynamically change its physical properties according to a user's input [5] (Figure 1).

Figure 1

An Artist's Rendition of Programmable Matter [6]

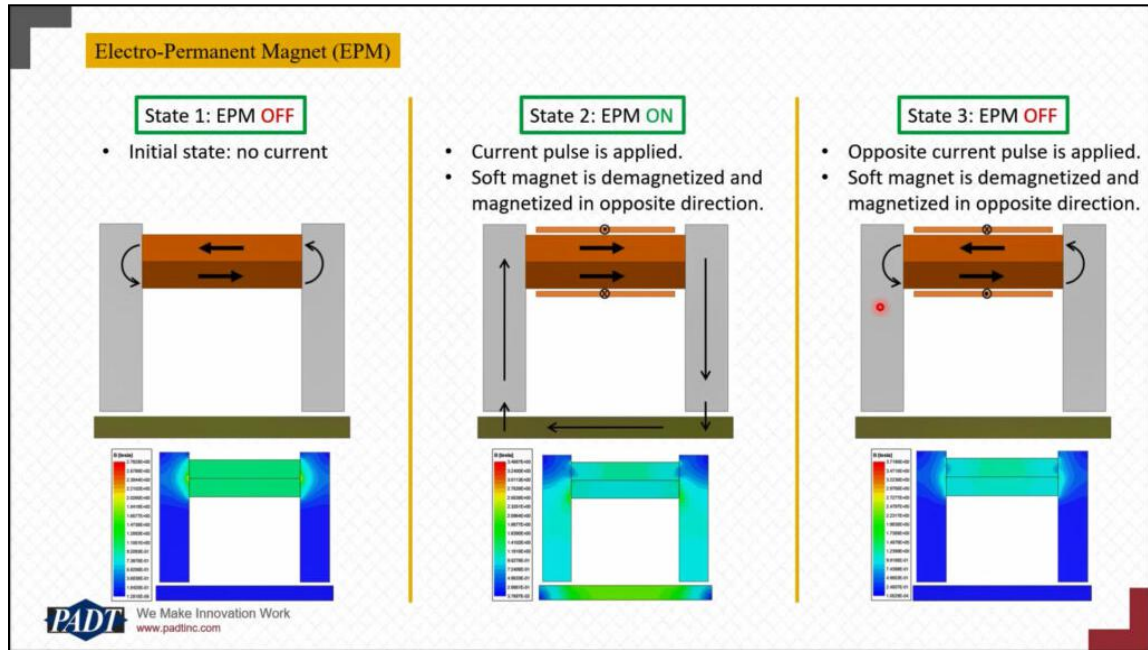


Over the last few decades, programmable matter research efforts have primarily centered around modular swarm robotic systems, where the interactions between individual robots

determine the swarm's physical properties, rather than their chemical compositions or inherent material characteristics [7]. Projects like soft-handed shearing auxetics at the Massachusetts Institute of Technology [8], Claytronics at Carnegie Mellon University [8], self-folding origami with the U.S. Defense Advanced Research Projects Agency [3], and VisibleSim at the FEMTO-ST Institute [9] are just a few different *modi operandi* already taken towards a final vision of programmable matter.

However, one common limiting factor is scale: in order for a discrete swarm system to convincingly behave as a continuous material, robots in the swarm must be as small as possible [10]. A comparison can be made to the pixels that make up a digital display, where the smaller the pixels are, the higher the resolution is, and the more realistic the produced image will seem to the human eye [11]. Until very recently, semiconductor process node technology was not advanced enough to realize microrobots much smaller than those previously mentioned. Today, the rapid microscaling of integrated circuits, which has already surpassed predictions and may soon approach fundamental limits, enables the development of complex sensing, computing, and actuating devices at the micrometer scale [12].

On top of sufficiently small integrated circuits, the volume occupied by actuating components in each microrobot should be kept to a minimum, because heat loss increases volumetrically and can significantly limit performance by increasing power draw and decreasing force output [7]. Though common in macroscale swarm systems, moving parts, like flywheels, motors, and telescoping arms, are incredibly difficult to downscale; operating small, weak devices under the influence of electrostatic forces demands constant maintenance and repair, which is not feasible for a semi-autonomous system like programmable matter [7]. One possible contender for a microscale, solid-state actuator is the electropermanent magnet (EPM), a device which is low power, simple to manufacture, and scales force exertion by area and force consumption by volume [13]. Electropermanence is a principle in which two magnets of vastly different coercivities are paired with each other in an electromagnetic configuration [14]. When a current too low to power the high coercivity, or hard, magnet, but high enough to saturate the low coercivity, or soft, magnet, is applied, only the soft magnet's magnetization is switched [14]. The net magnetic field of the system is thus either completely in one direction or zero (Figure 2).

Figure 2
Simulating Magnetization and Demagnetization of an Electropermanent Magnet [14]


By applying one short electrical pulse, an EPM can be easily switched on and off. Energy is a scarce, yet valuable resource in large-scale swarm systems, so it is ideal that no continuous current flow is necessary to maintain either the magnetic off or on state [15]. EPMs on the face of a microrobot would not only occupy very little internal volume, but allow it to connect to others at high strength, communicate with others through timed pulse processing and generation, and even power others through electromagnetic induction [16].

Because each microrobot must be completely solid-state, movement must be external to the system. Often, technology draws inspiration from existing natural and biological systems to approach problems in emerging fields [17]. Cells comprising a living body can be directly compared to microrobots comprising a swarm system, as both are uniform, communicative, and most importantly, motile [18]. The random migration of eukaryotic cells is described by Brownian motion, or the stochastic motion of small particles as stimulated by the internal energy of their surroundings with no preferential direction of flow [19]. At the microscale, swarms of solid particles tend to behave as fluids and gases do [20]. An artificial source of energy completely surrounding a programmable matter system could stimulate each microrobot into motion so that there exists a constant transfer of energy between them. The robotic subunits

could even be scaled down until no artificial energy source is necessary — the Brownian motion of air particles in the atmosphere would then serve as stimulation enough [21].

In a microrobotic device, certain control and logic requirements exist. There is little space available on each integrated circuit for memory, which is commonly the largest spatial burden on a chip [22]. Both read-only program memory and rewritable data memory must be kept to a minimum [7], requiring that both data transferred between robots and the functions each robot carries out be kept as simple as possible [23]. In the use of six face EPMs, each acting as a one-bit memory with only two possible states, a total of 64 data arrays exist. The only microrobot powered and programmed by a computer, designated the seed node, stores one array for each additional microrobot, or sprout node, in the swarm. From the seed to the last sprout, memory usage decreases linearly; if n robots exist in the swarm, each succeeding sprout will be tasked with remembering anywhere from $6n - 36n$ arrays [24]. Because the computer program developed in last year's science fair project assigned the role of seed to the single robot most internal to the final form, the sprouts with the most arrays to remember always connected to the seed first, while those with the least connected last [24]. Using this delegation, power availability will always be directly proportional to power draw [25].

1.2. Engineering Concentration

In last year's project, designs for a microrobot shell, complete with face cobalt-platinum and iron EPMs, face iron nodes, internal copper terminals and wiring, and an internal circuitry cavity were 3D modeled and converted to cross-sectional layer designs. Six hundred masks total were created by hand for the selective electrodeposition of all three metals and a wafer of microrobots was then fabricated and diced into individual shells [26]. Circuits were prototyped on breadboards and tested for functionality, as well as used to test different power- and memory-reducing algorithms in system. From this evaluation, application-specific integrated circuits (ASICs) were designed and testbenched in an online environment. A simulation and modeling computer application was developed to further examine global algorithms, especially in swarms of tens of thousands of robots. The modeling tool was programmed to take an input of geometric point data from any CAD drawing and translate it to arrays of binary magnet configurations, readable by each microrobot's ASIC chip. This process suffered from slow,

tedious fabrication procedures, lack of ASIC design and fabrication resources, and an intermediate level of algorithm development.

To create a commercially viable programmable matter system, the manufacturing process must be made simple, cost-effective, and automatic. A 3-way gantry crane was constructed to perform rapid electrodeposition of copper, iron, and cobalt-platinum onto a substrate through elastomeric masks. During setup, the substrate was calibrated with each mask, and vector position data was indexed on a central computer. Then, the computer autonomously stepped the crane through designs, mating the substrate to each mask at timed intervals and applying voltage to each electrolytic cell for a set amount of time. After each set of designs was deposited, the layer was planarized and lapped with dielectric. Elastomeric masks were created in a nanofabrication facility, through maskless lithography and reactive ion etching processes. These masks are reusable, improving cost and resource efficiency. Integrated circuit chips were fabricated in the same facility, using photolithography to develop a mask set and ion implantation to dope target areas of a silicon wafer. Because this method is so similar to that used to fabricate the microrobot shells, it may be possible to integrate the two steps into one in the future. This would greatly expedite the manufacture process and cut equipment costs by a significant amount. These considerations are critical in the introduction of any new technology, especially at the global scale of programmable matter.

Once a set of microrobot shells was fabricated using the crane, and bare die ASIC chips had been bonded to terminals inside of and physically encapsulated by each shell, the simulated microrobotic system was programmed to achieve target functionalities. Distributed, cluster-based self-reconfiguration and redeployment algorithms were developed to maximize the limited memory, power, and surface area available to each microrobot. Parallelization of serial anti-deadlocking and constructive solid geometry algorithms was also simulated and explored [27]. Deadlocking occurs when outer layers of microrobots connect before inner layers do, creating unreachable cavities in a form. It can be prevented by reversing outside-in disassembly steps in simulation for use in system. Constructive solid geometry is a memory-reducing technique, implemented in the data-packaging computer application, that uses Boolean operations to combine simple forms into complex ones. Connection, data transfer, and power transfer networks in simulation and in system were mapped, weight was added to the seed node, and both existing and novel assembly planning algorithms were populated across the swarm to

ensure every microrobot took the shortest, most energy-efficient path to its final location, every time [28]. Because each of these networks relied on direct contact between one or more robots, and every robot was interchangeable and unidentified, the physical topology of the swarm varied with each iteration. However, the logical topology, or the established links between each robot during or immediately after contact, was always the same, regardless of their initial and final locations [29]. This topology was optimized to minimize congestion, load time, and other factors so that the same algorithms could be interchanged for each new form.

2. Methodology

2.1. Materials

Aqueous copper acetate ($\text{Cu}_2(\text{OAc})_4(\text{H}_2\text{O})_2$, 99.0%), aqueous ferric acetate ($[\text{Fe}_3\text{O}(\text{OAc})_6(\text{H}_2\text{O})_3]\text{OAc}$, 99.0%), diamino-dinitro platinum ($\text{H}_4\text{N}_4\text{O}_4\text{Pt}$, 98.0%), aqueous cobalt sulfamate ($\text{CoSO}_4(\text{H}_2\text{O})_7$, 99.0%), hexamethyldisilazane ($\text{C}_6\text{H}_{19}\text{NSi}_2$, 99.0%), tetramethylammonium hydroxide ($\text{C}_4\text{H}_{13}\text{NO}$, 99.9%), acetone (CH_3COCH_3 , 99.5%), and phosphoric acid (H_3PO_4 , 99.0%) were purchased from Beantown Chemical Co. (New Hampshire, USA). Cobalt-platinum, iron, and copper metal feedstock were purchased from American Elements (California, USA). AZ 12XT photoresist, AZ 300 MIF developer, AZ 400T photoresist stripper, diborane p-type dopant gas (B_2H_6 , 99.0%), and phosphine n-type dopant gas (PH_3 , 99.0%) were purchased from MicroChemicals (Baden-Württemberg, Germany). All chemical agents were used as received, after consulting their material safety data sheets.

L293D motor driver ICs were purchased from Texas Instruments (Texas, USA) and used as received, after consulting their datasheet. Autodesk AutoCAD software, KLayout Layout Editor, Glade Electronic Design Automation software, and Nabity Nanometer Pattern Generation System were downloaded and used as received. A Laurell Tech WS-650 spin coater, a Bruker SF-100 Lightning maskless lithography system, an Oxford Plasmalab 100/ICP 180 reactive ion etch system, a MKS medium-energy ion implanter, and an AJA ATC Orion sputter system were used according to their user manuals.

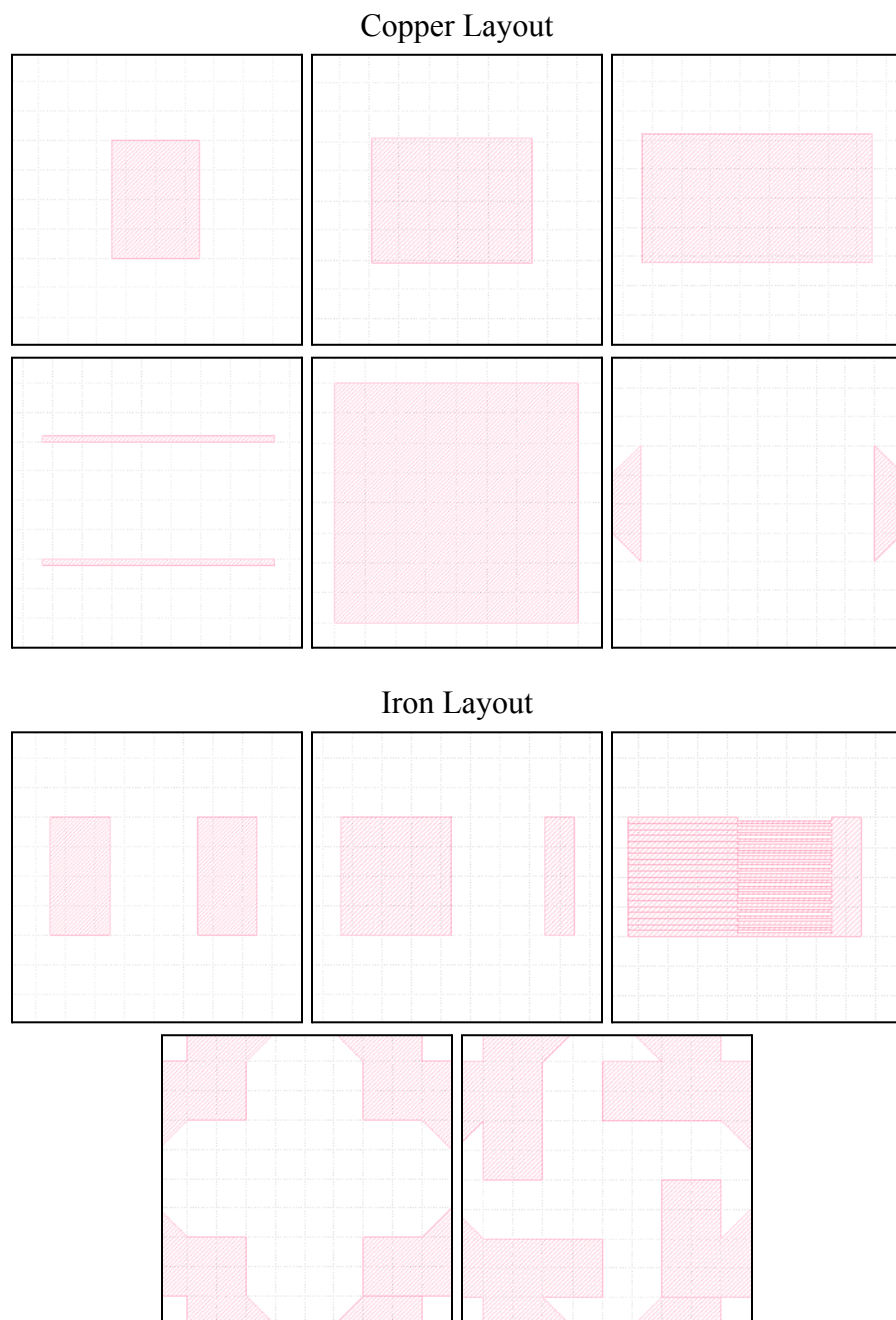
Elastomeric masks and integrated circuits were fabricated at the Rice University Shared Equipment Authority Nanofabrication Facility, under the supervision of PhD Fellow Sathvik Ajay Iyengar, in an ISO 5 process bay.

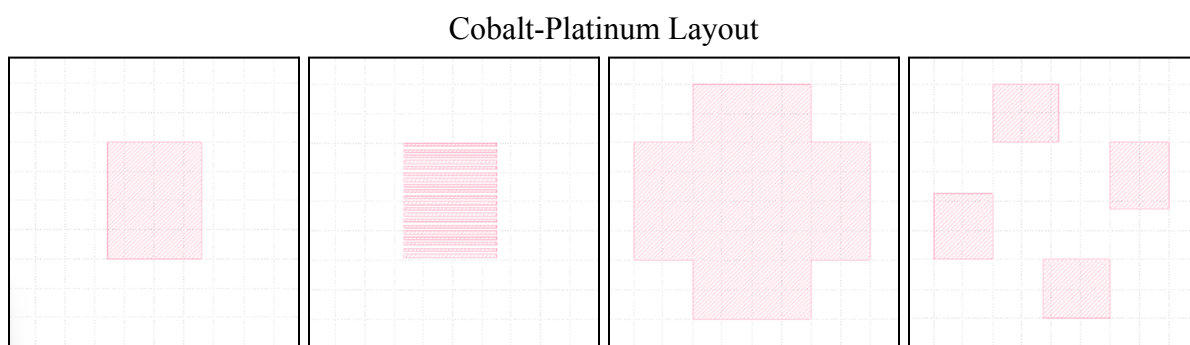
2.2. Elastomeric Mask Preparation

A microrobot shell was designed in AutoCAD, defining metal placement. Cross-sectional layer designs were generated in KLayout and exported into direct-write run files (Figure 3).

Figure 3

Cross-Sectional Layer Designs for Copper, Iron, and Cobalt-Platinum Deposition





Three silicon wafers were purified, spincoated with a 13 μm layer of photoresist, and baked dry at 100°C. Each design was written onto separate wafers using lithographic laser patterning. The wafers were immersed in developer to refine patterned features, rinsed with deionized (DI) water, and dried. The silicon of each wafer was etched 5 μm deep using inductively coupled plasma reactive ion etching (ICP-RIE). Any residual photoresist was stripped off and a 20 μm thick layer of anti-stick coating was deposited above the surface of each wafer. Each coating was hardened, cured, and detached from its wafer, creating three elastomeric masks: one for copper, one for iron, and one for cobalt-platinum deposition (Figure 4).

Figure 4

Scanning Electron Microscopy Image of an Elastomeric Mask

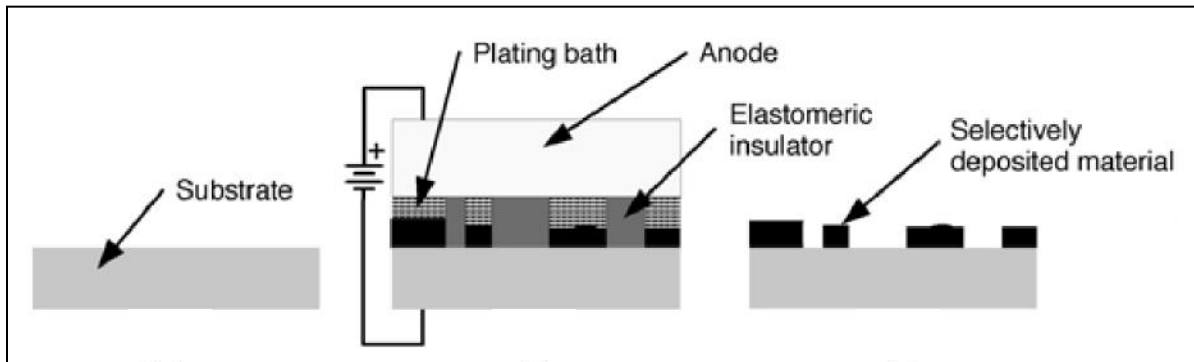


2.3. Three-Axis Gantry Assembly and Automation

A large steel casing was machined to house three insulating cells, each approximately 1 m³ in volume. One cell was filled with a copper acetate electrolyte solution and a partially-submerged copper metal feedstock; another with a ferric acetate electrolyte solution and a partially-submerged iron metal feedstock; and yet another with a cobalt sulfamate and diamino-dinitro platinum electrolyte solution and a partially-submerged cobalt-platinum metal feedstock [30, 31]. Metal feedstocks were sourced from high-purity scrubbing pads, loose coils, and wire, to maximize the surface area from which metal ions could migrate during electrodeposition [31]. A sheet of coarse sandpaper was fixed to the top of the steel casing, next to the electrochemical cells. Each elastomeric mask was immersed in its corresponding cell (Figure 5).

Figure 5

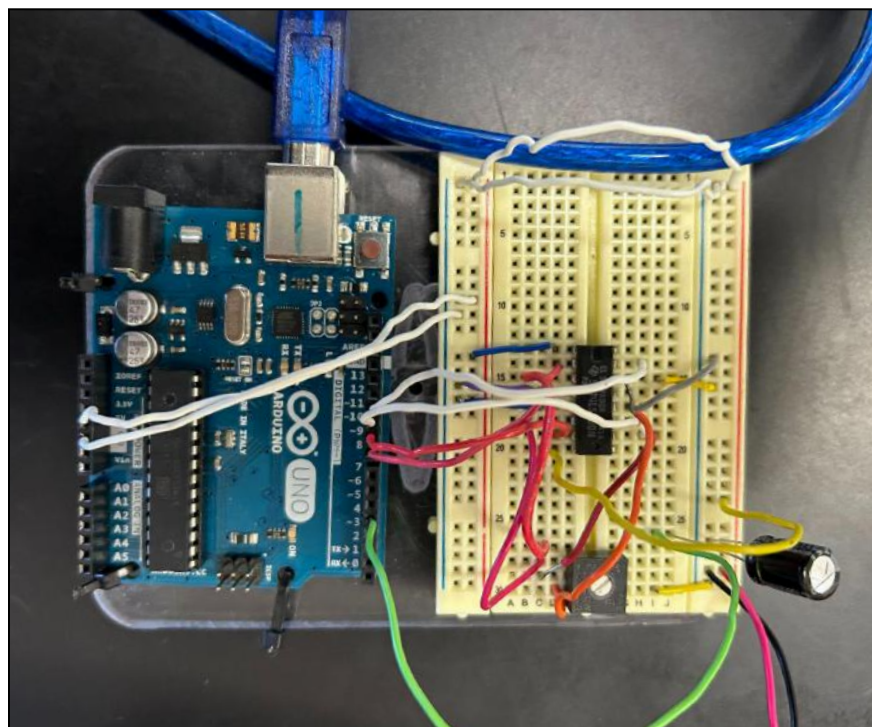
Electrodeposition Mechanism [32]



Five stepper motors were paired with five lead screws using couplings. Control circuits were built for each, using L293D motor driver chips, Arduino UNO boards, and a power source supplying the nominal voltage of each motor (Figure 6).

Figure 6

Bipolar Stepper Motor Control Circuit



The Arduino UNO boards communicated with a central computer for manual calibration and autonomous motion. The lead screws were arranged to allow linear motion on the x, y, and z axes, so that two ran parallel to the steel casing, two ran orthogonal to the casing, and one ran perpendicularly above the casing. A steel substrate was held by the latter lead screw. Finally, a 9 V battery was housed in the steel casing, so that the negative terminal was tied to the steel substrate and the positive terminal was bound to an unoccupied alligator clip.

2.4. Metal Shell Electrodeposition

To calibrate the gantry, the steel substrate was manually stepped across each elastomeric mask and coordinate position vectors for individual submasks were stored. The substrate was autonomously mated with each submask in each cell and a voltage was applied for a set amount of time: 2.4 s for copper, 1.8 s for iron, and 3.3 s for cobalt-platinum deposition. After each layer was deposited, dielectric was painted into the remaining cavities, heated with a heat gun, and cured. Then, the layer was planarized by having the substrate mate with sandpaper and step rapidly across it. The cycle continued until all 100 layers were deposited (Figure 7).

Figure 7

Deposited Metal Wafer, Cross-Hatched



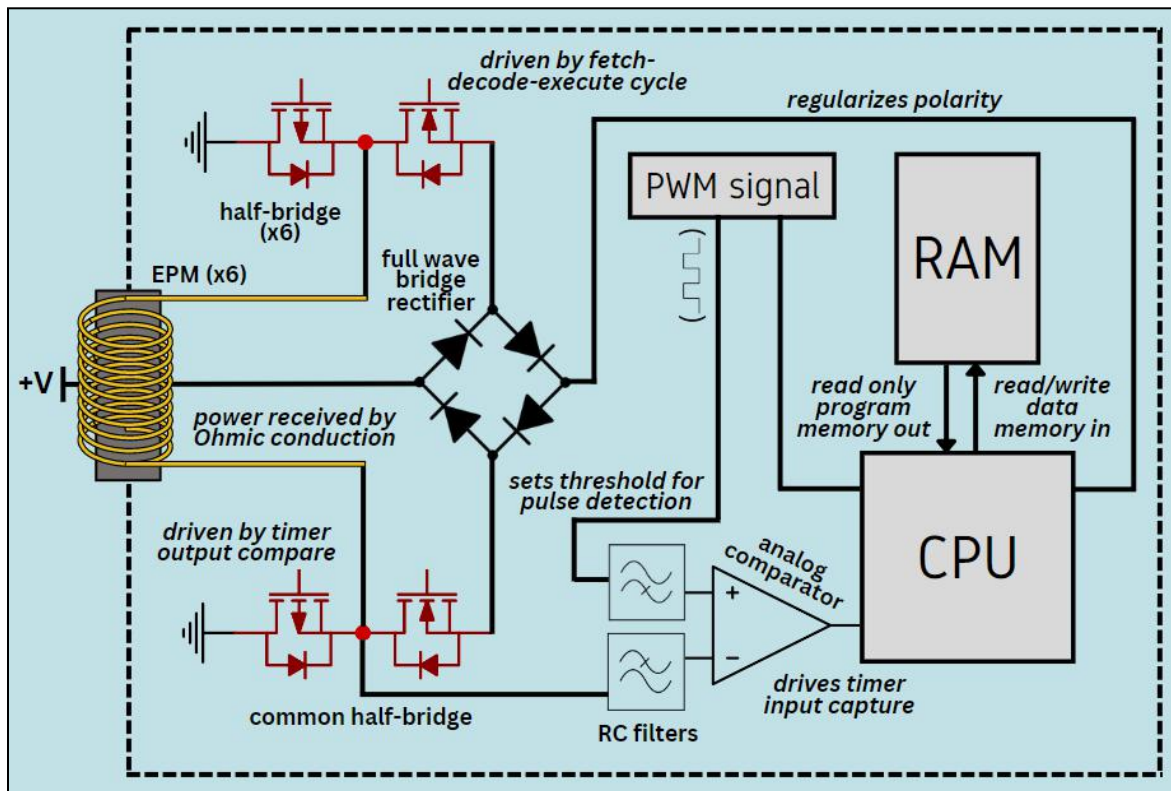
The metal wafer was detached from the substrate by splitting a sacrificial copper layer. The wafer was cross-hatched and pressure was evenly applied to dice and singulate 100 microrobot shell dies, each 500 μm tall. The dies were stored in a dark, cool room.

2.5. ASIC Design and Fabrication

High level functionality was described for an ASIC that produced ordered magnet drive pulses, sorted and acted on received magnet drive pulses, initiated, listened for and detected, processed, and responded appropriately to communication pulses, maintained both rewritable data memory and read-only program memory cells, performed rudimentary arithmetic necessary for time card calibration and protocol, and converted incoming power to a known polarity for internal use (Figure 8).

Figure 8

High Level ASIC Functionality Diagram



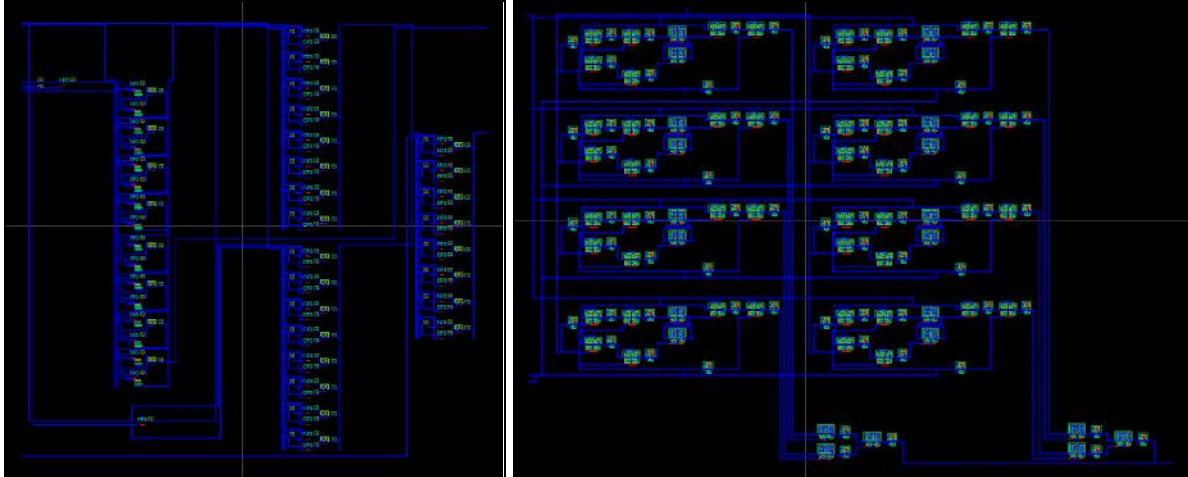
The ASIC was floorplanned and laid out in Glade. First, a library of compact logic gates was built. All transistors were placed, ensuring nodes were tightly packed but not inaccessible. Routing connections were initialized, and transistor placement was edited as necessary [33]. Terminals, input/output pins, and vdd! and vss! connections were added, and design rule check was used to verify the circuit design (Figure 9).

A testbench was developed for the design-under-test (DUT). All 64 possible array inputs were filed and injected into the testbench, and results were collected in a sister file. A golden output was written and manually compared to each real output. After each directed test, the DUT was modified and re-tested until the golden output was matched [34].

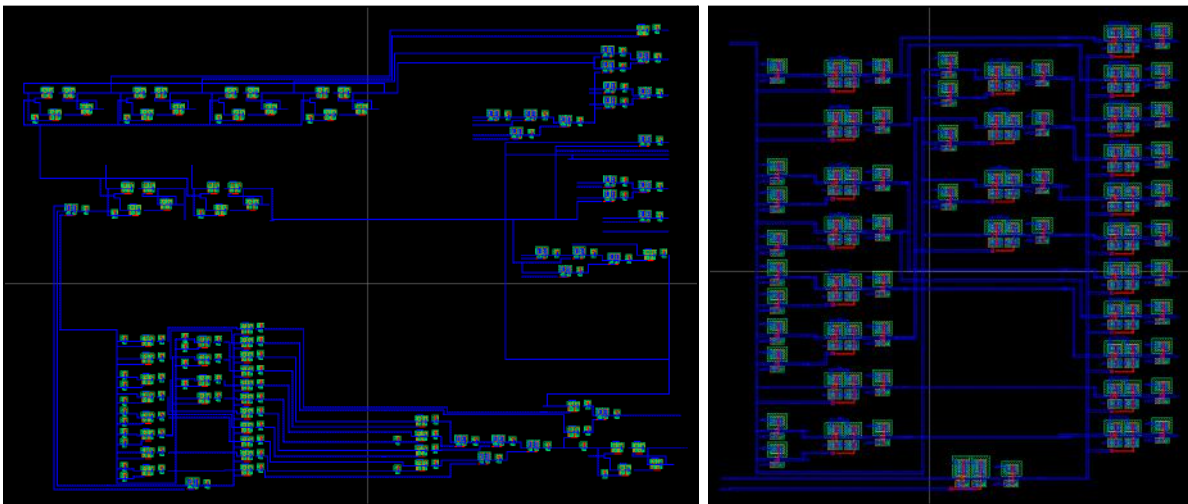
Figure 9

Key Elements of the Final ASIC

Arithmetic Logic Unit (ALU) and Random-Access Memory (RAM)



Instruction Decoder and Sequence Generator



Jump Logic



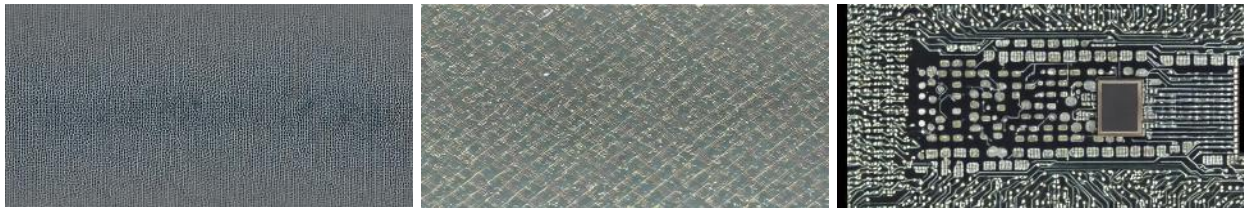
To fabricate ASIC chips, a bare 4 in. photomask was primed through dehydration and hexamethyldisilazane vapor deposition, then spincoated with an 8 μm layer of photoresist and baked dry at 100°C. The ASIC design was loaded into Nabity and patterned onto the photomask. The pattern was developed with a tetramethylammonium hydroxide and DI water (1:2 vol./vol.) chemical wash. Residual photoresist was stripped with an acetone wash, followed by an isopropyl alcohol wash, and the mask was cleaned with a high pressure DI water wash.

A silicon wafer was briefly baked, thermally oxidized, spincoated with photoresist, and baked dry. The photomask was optically reduced onto the surface of the wafer and the wafer was irradiated with UV light through the photomask. Residual photoresist was dissolved away.

The wafer was fed into the loading bay of an ion implanter. The bay was sealed, the diborane gas valve was opened, and the ion source power supply was turned on. The wafer was doped for around 11 minutes. Then, the diborane valve was closed and the phosphine gas valve was opened. The wafer was doped again, and dopants were alternated in this manner until all layers of the photomask had been set. The wafer was briefly baked and thermally oxidized. The wafer was metallized by sputtering aluminum at 500°C for 6 minutes, and the sputter target was etched with phosphoric acid through ICP-RIE (Figure 10).

Figure 10

ASIC Photomask, Wafer Shot, and Test Implementation



The wafer was singulated into 50 ASIC chips with a dicing saw. Each chip was tested for functionality by generating a fan-out oriented test pattern and probing for pulsed electrical output [36]. Chips were inserted into the microrobot shell dies, so that 50 dies were left vacant and 50 dies were occupied. Each vacant die was sealed over each occupied die with a thin layer of dielectric, so that 50 microrobots in total were created (Figure 11).

Figure 11

Microrobots Following ASIC Encapsulation



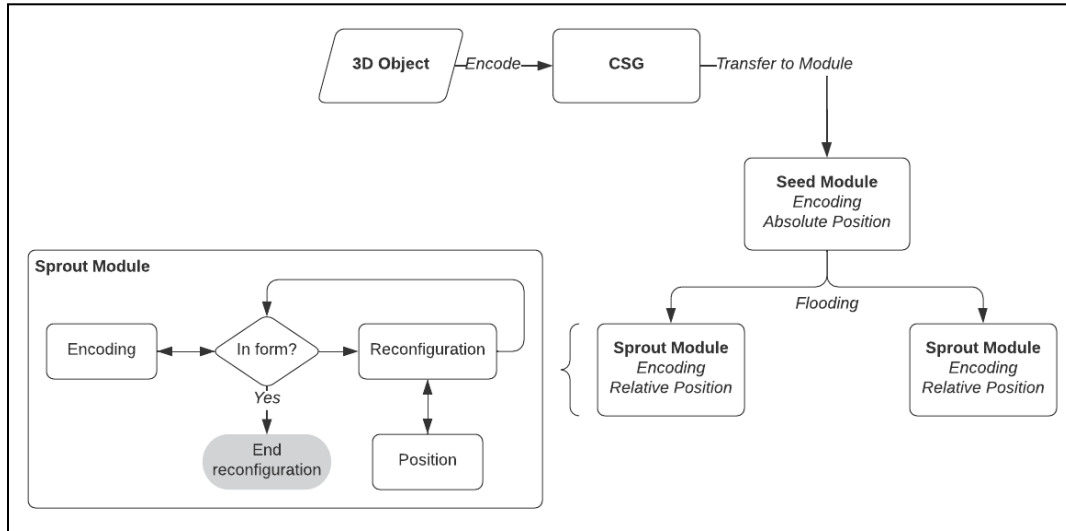
2.6. Application Software Expansion

A novel simulation and modeling program was further developed in Microsoft Visual Studio, using C++ and OpenGL. The front-end modeling platform, originally relying on primitive principles of 3D computer-aided design, was modified to include basic object generation and Boolean operations, better guiding user input [27]. Cached geometric point data from completed models was funneled through a pipeline of four main algorithms, two of which worked in tandem to convert each drawn point into bits and then encode them into generic EPM configuration arrays, and two of which reduced complexity along the way. The arrays were then converted for export to the read/write pin of an ASIC through the computer's command line, where they were read by the seed microrobot's chip. Data buses were calibrated according to the computer's inbuilt packet-based messaging scheme.

The program's simulation platform was optimized in a similar fashion: point data from models was processed and meshed through the 3D model, so that its volume was populated with a microrobot swarm form. Each microrobot was left unidentified and processes such as serial anti-deadlocking and constructive solid geometry (CSG) were newly implemented to aid in disassembling the form concentrically about the innermost microrobot (Figure 12).

Figure 12

CSG Implemented Into Reconfiguration Model Flow



Disassembly steps were reversed to simulate assembly of the form and speed and displacement statistics were displayed for each microrobot at the end of the simulation. Additional tools were implemented to optimize the complexity of the simulation, so that up to 100,000 nodes at once could be consistently tolerated in both assembly and disassembly run files.

2.7. Magnet-Fielded Stochastic Motion

A wooden platform was mounted to the plate of an orbital shaker. Rods of cobalt-platinum metal were fixed around the perimeter of the platform, alternating magnetic poles so that microrobots with at least one EPM activated were unable to exit the platform's bounds. When the orbital shaker was turned on, any microrobots in contact with the platform moved stochastically; externalizing motion saves energy by eliminating both the need to house actuators within microrobots and the need for microrobots to power themselves. Granular matter obeys principles of Brownian motion when made fluid through vibration, so the microrobots behaved as liquids and gases do [19].

2.8. Physical Examination

The geometry of one microrobot was created and pre-processed in Ansys Mechanical Finite Element Analysis (FEA) software. Materials were defined using Ansys library presets, and no customizations to properties were made. The model was meshed under a Global Size control

value of 0.5, which produced a number of elements ideal for cuboidal mesh density. Displacement constraints were set and surface pressure loads were applied. The deformed geometry was post-processed and contoured. This method was repeated for a cross-section of nine microrobots to analyze long-term physical effects of repeated intermodular interaction [2].

Microrobot EPMs were tested to determine average magnetic pull strength of the system. EPMs were momentarily activated by overwriting time card protocol [35] and a dynamometer was used to determine the breakaway force necessary to overcome the attraction between two activated EPMs (Figure 13).

Figure 13

Two Microrobots At Breakaway Point

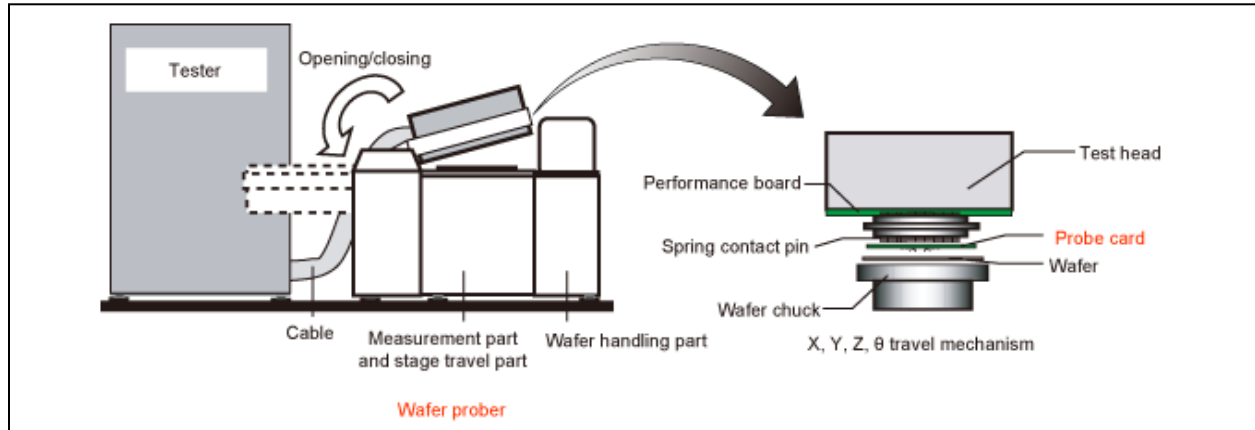


Integrity of electrodeposition was confirmed with a heat-quench test: sacrificial microrobot shells were heated in an oven and then doused in water. Shells were then examined under a microscope for evidence of flaking, peeling, or blistering.

To examine fabricated ASICs, a wafer probe test was performed (Figure 14). A probe needle transmitted patterned electric signals to each chip and returned data necessary to evaluate both response time and reliability of response.

Figure 14

Wafer Probe Test Process Flow [36]



Because speed of intermodular connection is not determined by pre-programmed motion planning algorithms, and rather by sprout nodes' proximity to each other and to the seed, it can only be tested in the physical system. All EPMs of one microrobot, the seed, were activated, and it was then introduced to a system of eight microrobots. the sprouts, each of which were powered off. Average time for each sprout to connect and reciprocate magnetic force through electromagnetic induction was logged. Because each ASIC stores time stamps for events, this was the most reliable way to map and analyze variations in connection speed in a nine-node system.

2.9. Logical Topology Optimization

A nine-node network topology was simulated in the developed computer program. In accordance with microrobot design, each node had six data transmitters and six data receivers. The topology was initially fully meshed and a direct label propagation algorithm was implemented to identify and remove the four datapaths with the lowest rate of transmission [29]. The amount of nodes in the network was then increased stepwise linearly and the datapaths removed in each increment were geometrically plotted to establish a region about the seed node with the lowest network throughput and the highest transmission delay.

Both time and space complexity of each topological algorithm were computed and solved for in O-notation. Energy use was simulated to scale logarithmically in relation to quantity of nodes online (microrobots in the swarm). This was experimentally verified by overloading the

simulated swarm with nodes until initial energy had completely dissipated, the form was left partially built, and at least one sprout on the outermost layer connected, but failed to power on.

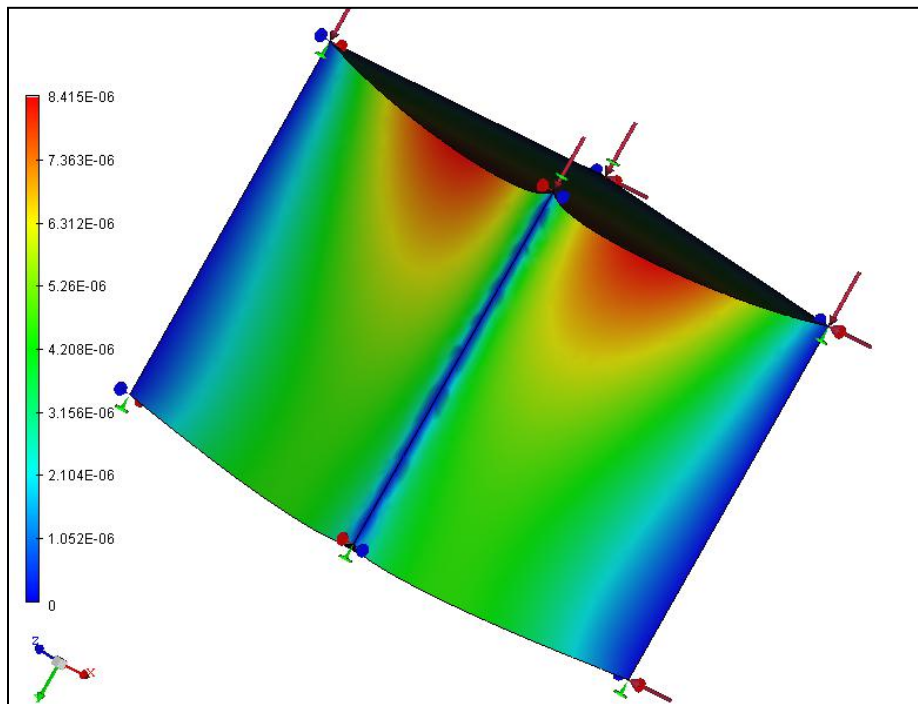
3. Results

3.1. Physical Characterization

Finite element method (FEM) is a useful technique for numerical characterization of complex bodies. Both a free microrobot and a cross-section of nine microrobots were modeled and von Mises equivalent stress was plotted across each (Figure 15). No outstanding loads were found.

Figure 15

Von Mises Stress on a Microrobot Following Agitation



Precision of electrodeposition at the microscale was verified periodically during shell fabrication. In no instance was evidence of flaking, peeling, or blistering found (Figure 16).

Figure 16

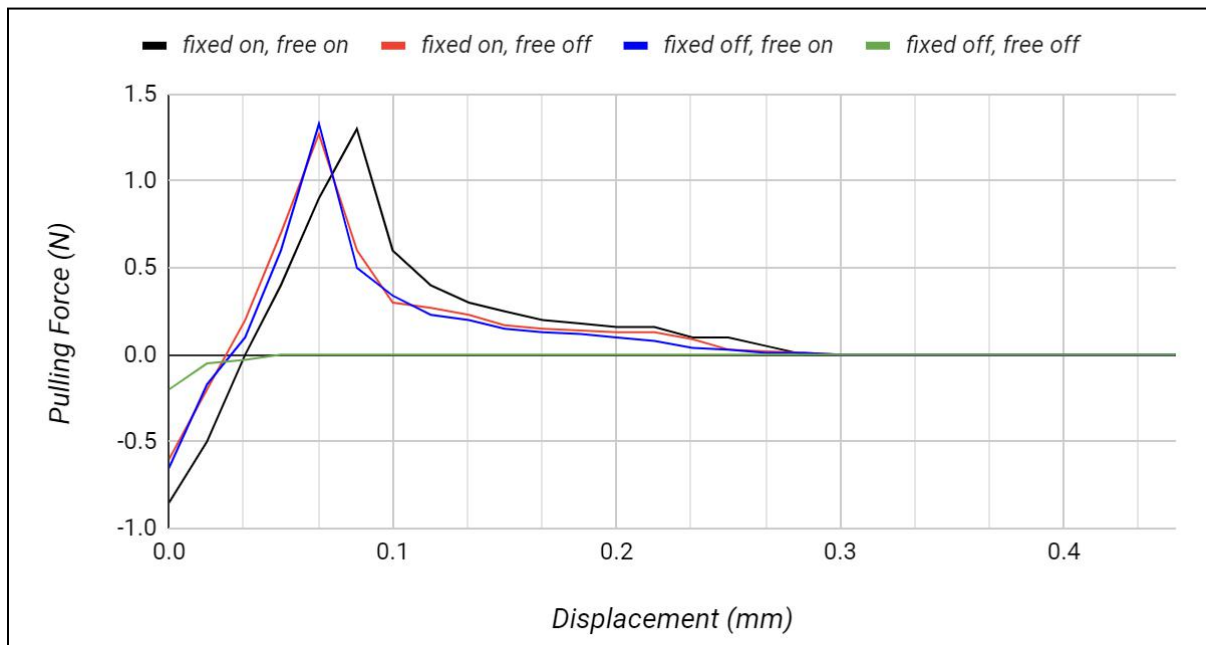
Evenness and Precision of Copper Deposition



To quantify the trade-off between intermodular connection strength and power draw, several magnet pull tests were performed between microrobots in the physical system. One microrobot was fixed to a level surface and a dynamometer was used to pull away a free, magnetically attracted microrobot parallel to the surface. Average pulling force was plotted against average displacement of the free microrobot (Figure 17). Breakaway force, or the minimum force necessary to disrupt a magnetic attraction between two microrobots, is represented by peaks in the plots below. Each of the plots can be integrated to find total work done.

Figure 17

Force vs. Displacement for Electropermanent Magnet Pull Tests



The data suggests a difference between breakaway force of on and off configurations, but not among different variations of on configurations. To further support this observation, a Kruskal-Wallis one-way analysis of variance (ANOVA) test was performed (Table 1). The breakaway force necessary to disconnect multiple microrobot pairs was determined. Different microrobots were cycled through to eliminate unique deformity as a potential source of error.

Table 1

Breakaway Force Kruskal-Wallis ANOVA Conditions and Results

Groups	fixed on, free on	fixed on, free off	fixed off, free on	fixed off, free off
Sample size (n)	18	18	18	18
Rank sum (R)	800.5	791.5	743.5	292.5
R^2/n	35600.014	34804.014	30710.681	4753.125
The test statistic H is 23.0216. The p-value is 0.00003997.				

While the Kruskal-Wallis ANOVA test served well to examine overall significance of difference between breakaway force in various configurations, Dunn's test was applied post-hoc to determine which specific configurations were significantly different in connection strength from each other (Table 2).

Table 2

Breakaway Force Dunn's Post-Hoc Conditions and Results

	fixed on, free off	fixed off, free on	fixed off, free off
fixed on, free on	0.5	3.17	28.22
fixed on, free off	0	2.67	27.72
fixed off, free on	2.67	0	25.06

The Bonferroni corrected α value is 0.008333. Since the p value is less than the corrected α value, the results of Dunn's post-hoc test can be considered.

3.2. ASIC Functionality

A testbench was used to examine input packages in every variation of process, supply voltage, and temperature (PVT) the ASIC design under test is expected to operate under (Table 3).

Table 3

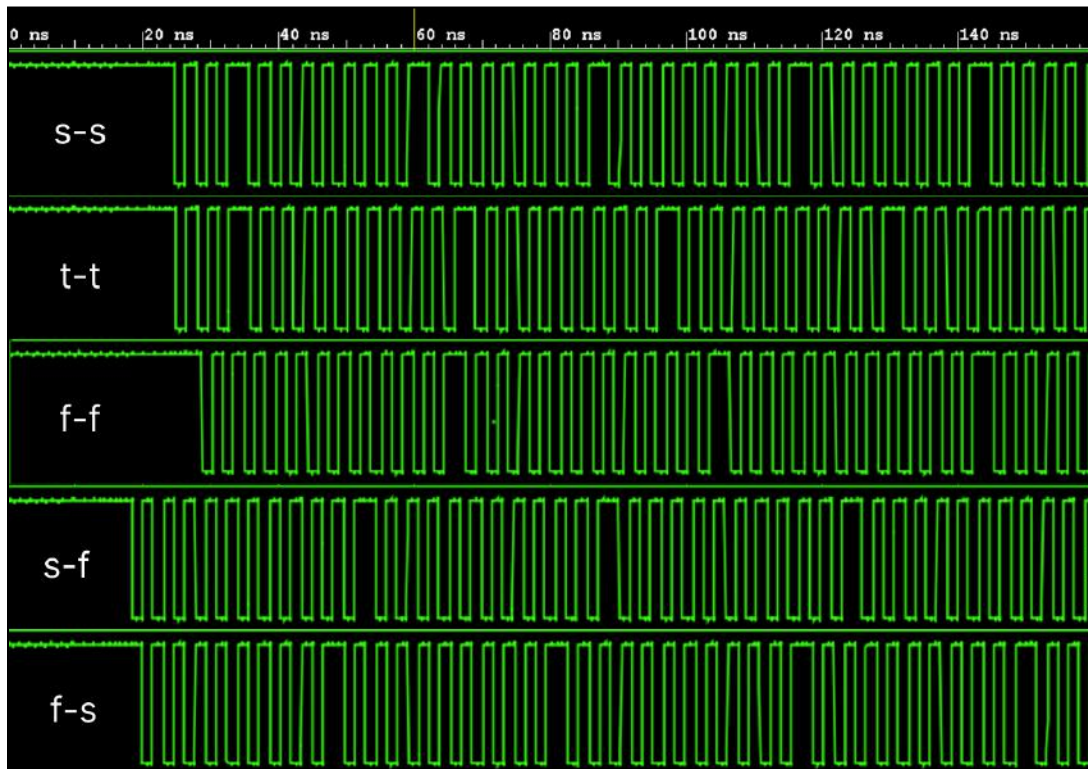
PVT Corners for Testbenching

Process	slow-slow	typical-typical	fast-fast	slow-fast	fast-slow
Supply voltage (V)	1.5	1.5	1.8	1.5	1.5
Temperature (°C)	100	50	-20	50	50

After assigning PVT conditions, a batch-mode simulation was run in the Glade EDA to perform 64 input/output trials for each. Results are shown below (Figure 18).

Figure 18

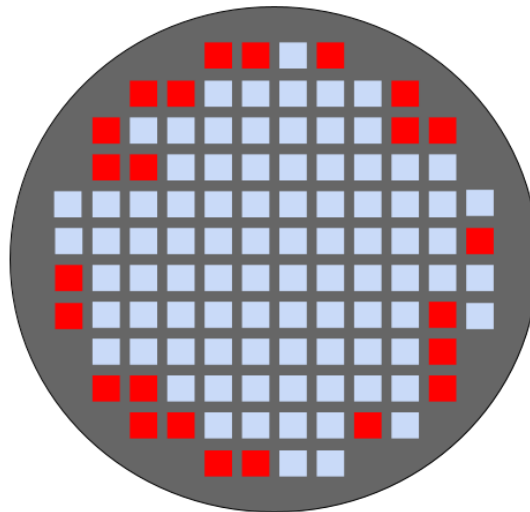
Q Outputs Across 5 Different PVT Corners



Functionality was tested and modified throughout the ASIC design process. However, some key characteristics were verified at the wafer level, post-development. All individual ASICs on the fabricated wafer were tested for functionality using fan-out oriented test pattern generation. The wafer was characterized and mapped; the locations of failed or faulty ASICs are indicated in red (Figure 19).

Figure 19

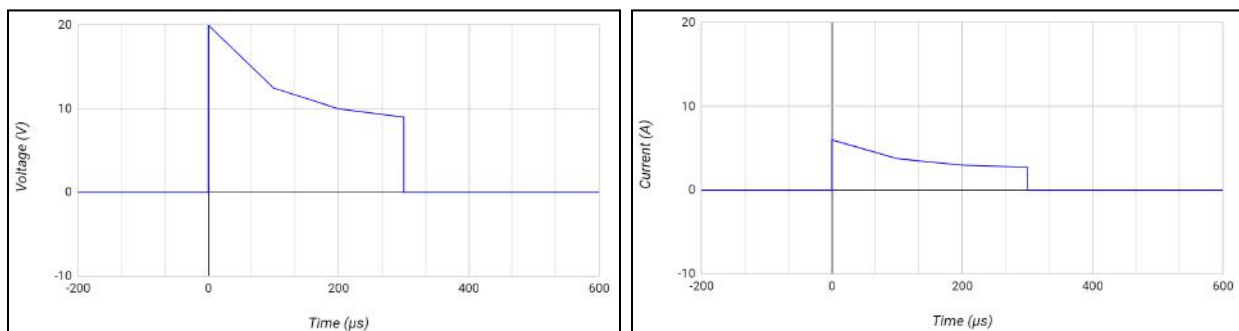
ASIC Wafer Bin Map



After the ASICs were implemented into the microrobots, voltage and current were measured on an EPM coil over the course of one communication pulse (Figure 20).

Figure 20

Voltage and Current Through an Electropermanent Magnet Coil



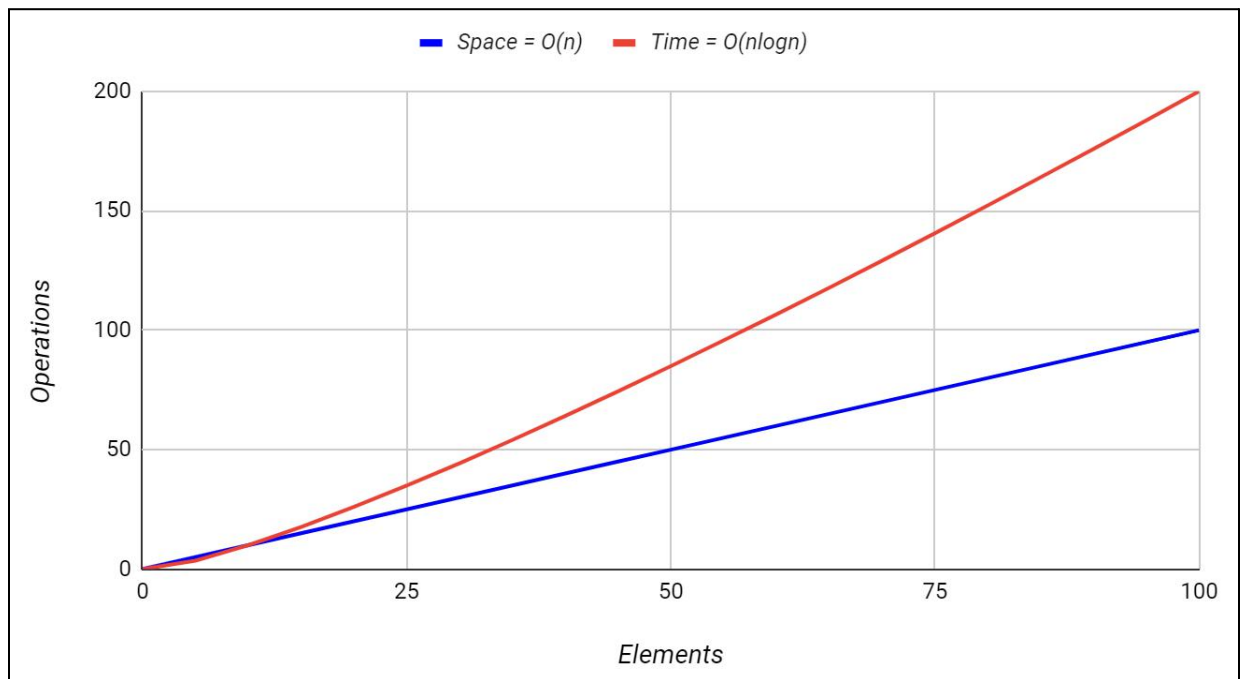
Voltage and current both peak, then decrease. This indicates that the microrobot EPMS did not fully saturate, and some base material limit or inefficiency may be hindering EPM saturation. Instead of by full magnetic saturation, peak current during each trial was restrained by the discharge rate of the ASIC's main capacitor.

3.3. Algorithmic Modeling

Time and space complexity of each novel motion planning, self-assembly, and topological optimization algorithm were solved for in O-notation (Figure 21).

Figure 21

Algorithmic Time and Space Complexity



Integrity of novel algorithms in system was examined for forms of varying size and complexity. Instances of deadlocking, faulty power distribution, and timed-out computation time are outlined below (Table 4).

Table 4

Mean Algorithm Integrity in Forms of Varying Size and Complexity

Form	Cube (small, simple)	Torus (small, complex)	Tower (large, simple)	Car body (large, complex)
% deadlocked	0%	0%	0.1%	0.4%
Idle nodes	0	0	0	0
Computation time (s)	22	38	56	78

Low transmission rate datapaths in swarms of increasing quantity were identified and removed in simulation. Removed datapaths were randomly shuffled to establish a common region across swarm sizes with lowest network throughput and highest data transmission delay.

Forms of varying size and complexity were overloaded with microrobots to identify the exact point of complete energy dissipation (Table 5).

Table 5

Mean Energy Dissipation in Forms of Varying Size and Complexity

Form	Cube (small, simple)	Torus (small, complex)	Tower (large, simple)	Car body (large, complex)
Dissipation time (s)	22	22	67	75
Final volume (nodes)	27	29	79	83

A difference was found between the volume of nodes remaining after forms of varying size were assembled, but not complexity. To determine if this difference is statistically significant, a one-way analysis of variance (ANOVA) test was performed (Table 6).

Table 6

Energy Dissipation ANOVA Conditions and Results

Source	DF	Sum of squares	Mean squares
Groups (between groups)	2	14485.33	7242.667
Error (within groups)	21	8	0.381
Total	23	14493.33	630.145

The f -ratio value is 19012.016. The p -value is 0.000001.

While the ANOVA test served well to examine overall significance of difference between energy dissipation in various forms, a Tukey-Kramer test was applied post-hoc to determine which specific forms were significantly different in dissipation rate from each other (Table 7). The results of this post-hoc test are valid because the prior ANOVA test yielded a statistically significant f -ratio value, and can therefore be considered.

Table 7

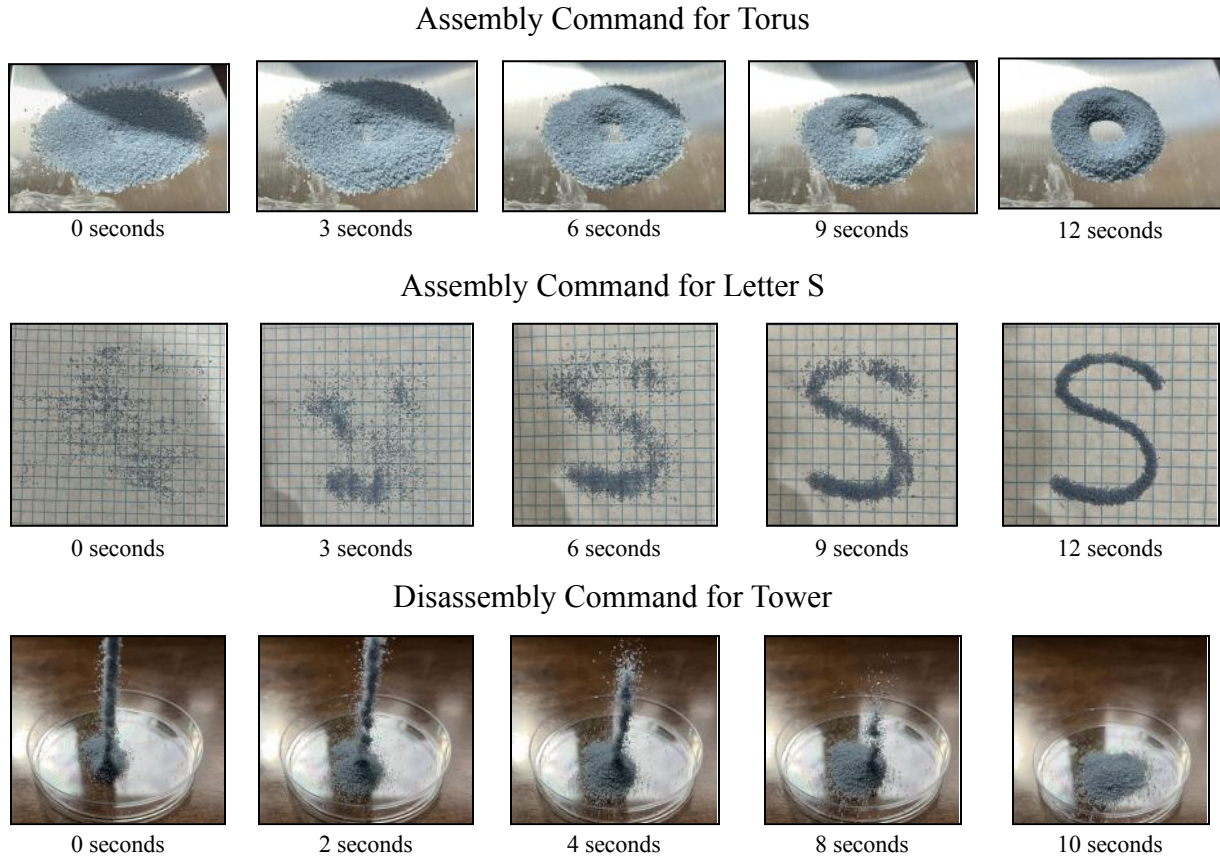
Energy Dissipation Tukey-Kramer Conditions and Results

Pairwise comparison	Critical value Q
Cube : Torus	8.5096 ($p = 0.10$)
Cube : Tower	226.9235 ($p = 2.862\text{e-}12$)
Cube : Car body	247.4592 ($p = 7.137\text{e-}13$)
Torus : Tower	235.4331 ($p = 2.862\text{e-}12$)
Torus : Car body	253.587 ($p = 2.862\text{e-}12$)
Tower : Car body	18.1539 ($p = 0.16$)

Finally, the trajectories of microrobots and encounter events were recorded and timestamped for a number of forms (Figure 22).

Figure 22

Trajectories of Microrobots and Encounter Events



4. Discussion

4.1. Analysis of Results

A modular microrobotic swarm was fabricated and tested for physical integrity, circuit functionality, and algorithmic adherence.

FEM was used to quantify displacement at various nodes of the microrobotic swarm. No outstanding loads were identified and von Mises yield criterion was met. Sources of electric and magnetic failure and loss were identified using auxiliary features of FEM. Periodic analyses during development and a final analysis afterwards helped ensure the microrobots would remain durable and functional after repeated use.

Strength of intermodular connection was tested for four different modes of EPM configuration, and the strength of connection between “fixed EPM on, free EPM off”, “fixed EPM off, free EPM on”, and “fixed EPM on, free EPM on” was found to not be significantly

different. However, the strength of connection between “fixed EPM off, free EPM off” was found to be significantly less than the other three configurations [$H = 23.0216$, $p < 0.0001$], with an average breakaway force of 0 N. The average breakaway force required to disrupt a secure intermodular connection is 1.03 Newtons, comparable to the weight of a computer mouse. Each EPM holds approximately 1,000 times its own weight; in a swarm, this strength scales with surface area. Therefore, extra energy does not need to be expended by reciprocating EPM connections. Handshaking algorithms can be instructed to inquire which EPMs the connected party has already activated, informing autonomous, real-time decisions.

PVT testbenching was performed to validate functionality of ASIC designs. Because every possible input produced its corresponding golden output, the final design was confirmed. The reference voltage used was 500 mV, and the output produced a maximum error of 4 mV, which is within acceptable range. Matching real output to golden output verifies the final ASIC design for fabrication and use.

Because many of the fabrication processes employed were experimental, checkpoints like electrodeposition heat-quench tests and ASIC wafer probe tests were set up to verify all

Pulse non-uniformity suggests that EPMs do not fully saturate during power and data transfer. This drain on power could be alleviated by implementing a double pulse; the time spent recharging the energy storage capacitor would be offset by the increased force of the second pulse. This would likely result in full EPM saturation and optimal material efficiency.

Algorithmic space complexity was found to scale linearly, indicating that the amount of space required by implemented algorithms increases at a 1:1 ratio to input elements. Because ASICs were architecturally optimized to occupy as little space in the microrobots as possible, and because memory is one of the biggest burdens on chip space, linear space complexity is optimal for the system. Time complexity was found to scale logarithmically; this may severely affect large-scale forms, warranting further time complexity reduction.

Self-reconfiguration and motion planning algorithms were applied to a variety of forms and all instances of poor performance were logged. Across forms, issues were never severe enough to inhibit assembly completely; the most prevalent issue, deadlocking, never surpassed 0.4%, even in the largest, most complex forms. This suggests the algorithms work well to prevent disorientation in the swarm.

The identification of low transmission rate datapaths in variously-sized swarms established the region immediately about the seed node as consistently low in throughput and high in delay. This can be attributed to the high volume of data input into the swarm and the low number of microrobots available to initially transfer it. Geographical awareness of this region helps in setting constraints for novel topology algorithms and localized data flow.

Energy distribution in the swarm was modeled as a flow field, and energy dissipation was calculated by overloading the swarm with additional microrobots. Energy dissipated at higher rates in forms of increasing size, but did not in forms of increasing complexity. This difference was found to be statistically significant [$F(2, 21) = 19012.016, p < 0.00001$]. This suggests that the same power feed can be used for every form of n size, regardless of complexity. Additionally, this validates constructive solid geometry algorithms in both simulation and system.

As a final compliance test, the microrobots were instructed to self-reconfigure into a number of forms. Every form was appropriately created, within a reasonable amount of time. Testing self-reconfiguration of large-scale forms was restricted to the computer simulation, because under 100 microrobots were physically fabricated and available for use.

4.2. Limitations

Due to age-related and financial restrictions, the researcher had limited access to laboratory space and equipment. Though elastomeric masks and ASICs were fabricated in a university cleanroom, all other fabrication and testing was performed in a household garage. The integrity of the fabricated swarm may have been compromised by ferromagnetic contamination and other particulate matter present in the garage. Around 60% of garage airflow was directed to a glove box to reduce error, but cleanroom conditions could not be sufficiently replicated. When testing microrobotic components besides elastomeric masks and ASICs, equipment used was low-precision and not intended for fabrication at the microscale.

4.3. Future Work

FEM revealed three loss mechanisms present in the microrobot swarm: I^2R loss, hysteresis loss, and elastic loss. While speculations can be made about the causes of these phenomena, mathematical investigation is necessary to minimize loss and optimize power usage. I^2R loss due to electrical resistance is simple to solve, using Ohm's Law and the standard power loss equation. Resistance across nodes in a microrobot could be measured using a multimeter;

current is already known. Elastic loss due to intermodular collisions can be solved with a mean-field approximation, assuming loss is attributed to interactions between microrobots and thus described by a single collision probability value. A Monte Carlo simulation might also suffice, considering the motion of microrobots prior to activation stochastic and unbound by external obstacles like walls. Hysteresis loss due to repeated magnetic agitation of face EPMs can be modeled using a B-H curve. However, EPM magnetization is reversed at relatively low frequencies (at most, 2 Hz), so hysteresis loss is likely not a major source of loss.

In any lattice architecture, nodes of interest exist [37, 38]; in this system, there is only one. Relying on only the seed microrobot to power and program the entire swarm, especially in large-scale applications, invites the possibility of total assembly failure due to a flaw in the seed. Network redundancy is a potential solution, because if one seed node fails, other seed nodes in the system are able to effectively replace it. Local clustering algorithms could be written, using Voronoi tessellations and nearest-neighbor theory, to assign a hierarchical government system across the swarm. As an added bonus, scaling seed node quantities with swarm size would increase available memory space, power feed, and speed of assembly.

Manufacture of the microrobots should be further streamlined for boosted scalability and commercial viability. Because the maskless lithography-electrodeposition method used to fabricate microrobot shells is so similar to the photolithography-ion implantation method used to fabricate their internal ASICs, it may be possible to integrate the two steps into one in the future. One outstanding issue with integration is that certain corrosive chemicals are used during integrated circuit fabrication that may react detrimentally with the elastomeric masks or newly-electrodeposited metal shells. However, if this issue was overcome, integration would greatly expedite the manufacture process and cut equipment costs by a significant amount.

A significant step in the advancement of programmable matter is downscaling. The current swarm can run on an 180 nm node process or lower, but eventually, the smallest transistor processes will dictate the smallest microrobots possible, because ASICs occupy the largest volume in each. Further research and development in silicon technology will be pivotal. The most apparent benefit to downscaling is enhanced structural integrity of conformations; because more microrobots packed into the same volume increases EPM holding force, smaller modules will allow for higher levels of unity. Another promising possibility is replacing the root of motion, previously an artificial, magnet-fielded stochastic environment, with the natural

Brownian motion of gas particles in the atmosphere to autonomously agitate and actuate the system. Not only does this reduce energy input to nearly zero, but it opens up the ability to use programmable matter anywhere, without being limited to the constraints of an artificial environment.

4.4. Concluding Remarks

The developed microrobotic swarm operates at high functionality, using electropermanent magnets for strong connection and rapid data and power transfer between nodes. The fabrication process combines age-old principles of electrochemistry with cutting-edge photolithographic technique, is scalable and streamlined, and generates large amounts of microrobots with little feedstock input. Integrated circuit designs are compliant and space-efficient, and both read-only and rewritable algorithms prevent common self-reconfiguration issues from occurring across forms of varying complexity and size. The developed computer program is able to smoothly simulate interactions between up to 100,000 microrobots and acts as a high-precision algorithmic test environment. The modeling function processes 3D, user-drawn models into configuration data recognized by microrobot chips, enabling human-driven, self-reconfigurable programmable matter.

References

- [1] Ekblaw, A. (2020, August 17). *Self-Aware Self-Assembly for Space Architecture: Growth Paradigms for In-Space Manufacturing* [Doctoral thesis, Massachusetts Institute of Technology]. DSpace@MIT.
 - [2] Park, S.-M. & Kim, Y.-G. (2022, January 04). A Metaverse: Taxonomy, Components, Applications, and Open Challenges. *Institute of Electrical and Electronics Engineers Access*, 10, 4209-4251.
 - [3] Goldstein, S. C. & Lee, P. (2006, August 17). *Realizing Programmable Matter* [Powerpoint slides]. U.S. Defense Advanced Research Projects Agency Information Science and Technology Study Group.
 - [4] McCarthy, W. (2003). *Hacking Matter*. Basic Books.
 - [5] Margolus, N. & Toffoli, T. (1987). Cellular Automata Machines. *Complex Systems*, 1(1987), 967-993.
 - [6] Ball, P. (2014, May 27). *Make Your Own World With Programmable Matter*. IEEE Spectrum.
 - [7] Knaian, A. N. (2010, May 21). *Electropermanent Magnetic Connectors and Actuators: Devices and Their Application in Programmable Matter* [Doctoral thesis, Massachusetts Institute of Technology]. DSpace@MIT.
 - [8] Alba, M. (2017, May 23). *The Promise and Peril of Programmable Matter*. Engineering. <https://www.engineering.com/story/the-promise-and-peril-of-programmable-matter>
 - [9] Chennareddy, S. S. R., Agrawal, A., & Karuppiah, A. (2017, March 15). Modular Self-Reconfigurable Robotic Systems: A Survey on Hardware Architectures. *Hindawi Journal of Robotics*, 2017.
 - [10] Capolino, F. (2009). *Theory and Phenomena of Metamaterials*. CRC Press LLC.
 - [11] Sutherland, I. E. (1965). *The Ultimate Display* [Paper presentation]. International Federation for Information Processing Congress, New York City, NY, United States.
 - [12] Kaku, M. (2012, May 01). *The End of Silicon-Based Computing* [Interview]. The Daily Galaxy.
 - [13] Mártonová, V. (2019, January). *Electropermanent Magnet Study* [Bachelor's thesis, Czech Technical University]. CTU Digital Library.
-

-
- [14] Liu, X. (2004, November). The Mechanics of Machining at the Microscale: Assessment of the Current State of the Science. *Journal of Manufacturing Science and Engineering*, 126(4).
- [15] McEvoy, M. & Correll, N. (2015, March). Materials that couple sensing, actuation, computation, and communication. *Science*, 347(6228).
- [16] Cannon, B. L., Hoburg, J. F., Stancil, D. D., & Goldstein, S. C. (2009, July). Magnetic Resonant Coupling As a Potential Means for Wireless Power Transfer to Multiple Small Receivers. *IEEE Transactions on Power Electronics*, 24(7), 1819-1825.
- [17] Cheung, K. C., Demaine, E. D., Bachrach, J. R., & Griffith, S. (2011, August). Programmable Assembly With Universally Foldable Strings (Moteins). *IEEE Transactions on Robotics*, 27(4), 718-729.
- [18] Wu, P.-H., Giri, A., Sun, S. X., & Wirtz, D. (2014, March 04). Three-dimensional cell migration does not follow a random walk. *Proceedings of the National Academy of Sciences*, 111(11), 3949-3954.
- [19] Feynman, R. P. (1962, April 20). *Brownian Motion* [Lecture 41A]. California Institute of Technology, Pasadena, CA, United States.
- [20] Lu, X., Zhao, Y., & Dennis, D. J. C. (2020, May 07). Fluid flow characterisation in randomly packed microscale porous beds with different sphere sizes using micro-particle image velocimetry. *Experimental Thermal and Fluid Science*, 118, 110-136.
- [21] Hughes, D., Heckman, C., & Correll, N. (2019, June 13). Materials that make robots smart. *The International Journal of Robotics Research*, 38(12), 1338-1351.
- [22] Lengiewicz, J. & Hołobut, P. (2018, February 16). Efficient collective shape shifting and locomotion of massively-modular robotic structures. *Autonomous Robots*, 2019(43), 97-122.
- [23] Navarro, I. & Matía, F. (2012, September 04). An Introduction to Swarm Robotics. *International Scholarly Research Notices*, 2013.
- [24] Schranz, M., Umlauft, M., Sende, M., & Elmenreich, W. (2020, April 02). Swarm Robotic Behaviors and Current Applications. *Frontiers in Robotics and Artificial Intelligence*, 7.
-

-
- [25] Aziz, F. I. B. A., Mamun, M., Bhuiyan, M. A. S., & Bakar, A. A. A. (2013, March 21). A Low Drop-Out Voltage Regulator in 0.18 μm CMOS Technology. *Modern Applied Science*, 7(4).
- [26] Cohen, A., Zhang, G., Tseng, F.-G., Mansfeld, F., Frodis, U., & Will, P. (1998). *EFAB: Batch Production of Functional, Fully-Dense Metal Parts with Micron-Scale Features* [Paper presentation]. International Solid Freeform Fabrication Symposium, Austin, TX, United States.
- [27] Lakhlef, H., Bourgeois, J., & Mabed, H. (2021, May 10). *Robust Parallel Redeployment Algorithm for MEMS Microrobots* [Paper presentation]. IEEE International Conference on Advanced Information Networking and Applications, Victoria, BC, Canada.
- [28] Calderón-Arce, C. & Solis-Ortega, R. (2019). Swarm Robotics and Rapidly Exploring Random Graph Algorithms Applied to Environment Exploration and Path Planning. *International Journal of Advanced Computer Science and Applications*, 10(5), 692-702.
- [29] Lee, K.-I. & Shayman, M. (2003, March). *A Local Optimization Algorithm for Logical Topology Design and Traffic Grooming in IP over WDM Networks*. Defense Technical Information Center.
- [30] Wang, Y., Jimenez, B. Y., Smith, C. S., Rendon-Hernandez, A. A., Samman, J., & Arnold, D. P. (2021, July 26). Microfabricated Electro-permanent Magnets Using AlNiCo and CoPt. *IEEE Magnetic Letters*, 12.
- [31] Wang, Y., Ewing, J., & Arnold, D. P. (2018, June 03). *Increasing the Thickness and Deposition Rate of High-Performance Electroplated CoPt Permanent Magnets* [Workshop]. Solid-State Sensors, Actuators and Microsystems Workshop, Hilton Head Island, SC, United States.
- [32] Cohen, A. L. (2002). *Electrochemical Fabrication (EFABTM)*. CRC Press LLC.
- [33] Djigbenou, J., Jagasivaman, M., & Fei, J. (n.d.). *Layout with Virtuoso*. https://www.mics.ece.vt.edu/ICDesign/Tutorials/Cadence/layout_pg1.html
- [34] Aung, N. (2021). *Integration of a Dynamic Offset Testbench in 0.18 μm CMOS to Measure Comparator Offsets* [Master's Thesis, California State University Sacramento]. CSUS University Library.
-

-
- [35] Romanishin, J. W. (2018, May 17). *M-Blocks: Three Dimensional Modular Self-Reconfigurable Robots* [Master's Thesis, Massachusetts Institute of Technology]. DSpace@MIT.
- [36] Micronics Japan Co., Ltd. (n.d.). *What is a wafer prober?* MJC Technical Column. mjc.co.jp/en/technology/column/wafer_prober.html
- [37] Mayya, S., Pierpaoli, P., Nair, G., & Egerstedt, M. (2017). *Collisions as Information Sources in Densely Packed Multi-Robot Systems Under Mean-Field Approximations* [Paper presentation]. Robotics: Science and Systems, Atlanta, GA, USA.
- [38] White, P., Zykov, V., Bongard, J., & Lipson, H. (2005, June). *Three Dimensional Stochastic Reconfiguration of Modular Robots* [Lecture transcript]. Robotics: Science and Systems, Cambridge, MA, United States.

Graphics statement: Unless otherwise cited, all graphics were created by the researcher.
